Implementation of a Silver Iodide Cloud-Seeding Parameterization in WRF. Part II: 3D Simulations of Actual Seeding Events and Sensitivity Tests

LULIN XUE, SARAH A. TESSENDORF, ERIC NELSON, ROY RASMUSSEN, AND DANIEL BREED

National Center for Atmospheric Research, Boulder, Colorado*

SHAUN PARKINSON, PAT HOLBROOK, AND DEREK BLESTRUD

Idaho Power Company, Boise, Idaho

(Manuscript received 5 June 2012, in final form 26 November 2012)

ABSTRACT

Four cloud-seeding cases over southern Idaho during the 2010/11 winter season have been simulated by the Weather Research and Forecasting (WRF) model using the coupled silver iodide (AgI) cloud-seeding scheme that was described in Part I. The seeding effects of both ground-based and airborne seeding as well as the impacts of model physics, seeding rates, location, timing, and cloud properties on seeding effects have been investigated. The results were compared with those from Part I and showed the following: 1) For the four cases tested in this study, control simulations driven by the Real-Time Four Dimensional Data Assimilation (RTFDDA) WRF forecast data generated more realistic atmospheric conditions and precipitation patterns than those driven by the North America Regional Reanalysis data. Sensitivity experiments therefore used the RTFDDA data. 2) Glaciogenic cloud seeding increased orographic precipitation by less than 1% over the simulation domain, including the Snake River basin, and by up to 5% over the target areas. The local values of the relative precipitation enhancement by seeding were ~20%. Most of the enhancement came from vapor depletion. 3) The seeding effect was inversely related to the natural precipitation efficiency but was positively related to seeding rates. 4) Airborne seeding is generally more efficient than ground-based seeding in terms of targeting, but its efficiency depends on local meteorological conditions. 5) The normalized seeding effects ranged from 0.4 to 1.6 under various conditions for a certain seeding event.

1. Introduction

The National Research Council (2003) provided two recommendations on numerical modeling efforts related to intentional weather modification: 1) improving cloud model treatment of cloud and precipitation physics, and 2) improving and using current computational and data assimilation capabilities. During the last decade, rapid progress has been made in these two areas. For example, the Wyoming Weather Modification Pilot Program (WWMPP; Breed et al. 2011) applied a state-of-art weather forecast system, the Real-Time Four Dimensional Data Assimilation (RTFDDA) Weather Research and Forecasting (WRF) model (Liu et al. 2008), to assist in the case-calling decision and the evaluation of seeding effects. Few if any studies have explored detailed seeding effects, however, and particularly forecasts of seeding effects. Such attempts require a microphysics scheme with the capability to simulate seeding events under realistic conditions.

In the first paper of this two-part series (Xue et al. 2013, hereinafter Part I), we demonstrated that a silver iodide (AgI) cloud-seeding parameterization coupled with the Thompson micropyhysics scheme (Thompson et al. 2004, 2008) reasonably simulated glaciogenic seeding effects of orographic clouds from ground-based generators and aircraft in an idealized two-dimensional (2D) model setup. The results indicated that, for stably stratified orographic clouds, AgI particles nucleated ice crystals mainly through deposition and enhanced precipitation amount under most of the seeding conditions. The majority of precipitation enhancement came from

* The National Center for Atmospheric Research is sponsored by the National Science Foundation.

Corresponding author address: Lulin Xue, National Center for Atmospheric Research, P.O. Box 3000, Boulder, CO 80307.
E-mail: xuel@ucar.edu

DOI: 10.1175/JAMC-D-12-0149.1

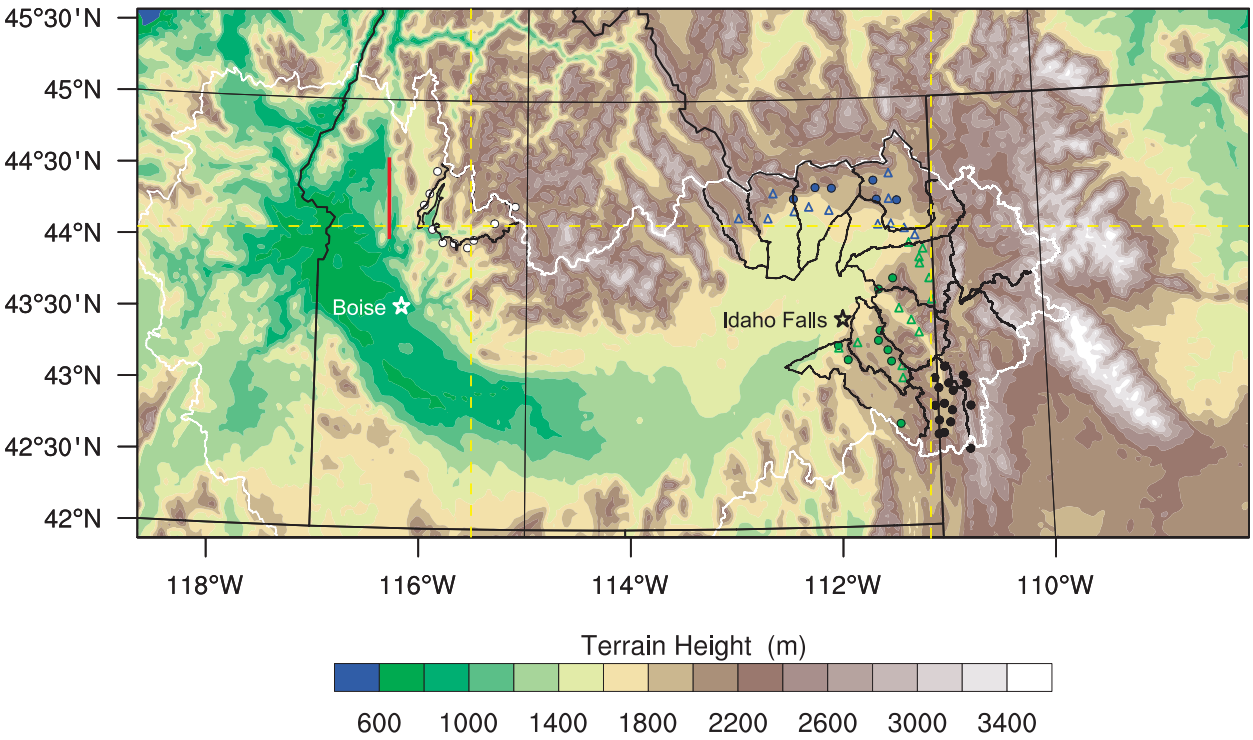

FIG. 1. Domain of the simulations. Terrain height (m) is color shaded. The Snake River basin is outlined in white. The Payette watershed and the eastern Idaho watersheds are outlined in black. Generators are indicated by circles (automatic generators with seeding rate of 20 g h^{-1}) and triangles (manual generators with seeding rate of 14 g h^{-1}). Generators over the Payette region are in white. Blue generators consist of the northern group over the target area in eastern Idaho (NEID in Table 1). Green is the southern group. Black is the Wyoming group (WYO in Table 1). White and black stars indicate the cities of Boise and Idaho Falls, respectively. Flight track A4B is represented by the red segment on the western side of the Payette watershed. The cross sections illustrated in Fig. 5 are indicated by yellow dashed lines.

vapor depletion rather than liquid water consumption. The seeding effect was found to be inversely related to the natural precipitation efficiency and was positively related to seeding rates. Airborne seeding enhanced precipitation on the upwind slope, and ground-based seeding increased precipitation on the downwind slope most of the time. In general, airborne seeding was more effective than ground-based seeding because of the improved targeting of the AgI to optimum cloud regions for snow growth and fallout.

As discussed in Part I, the 2D domain and smooth topography limited the AgI particle dispersion and the turbulence in the simulations, which arbitrarily enhanced the immersion-freezing mode and spillover ratio. In Part II (this paper), a three-dimensional (3D) domain with real topography is used to alleviate model artifacts in assessing seeding effects during actual seeding events. This study examines the wintertime glaciogenic cloud-seeding effects using the model under realistic conditions, including testing seeding sensitivities, comparing them with those found in 2D idealized simulations, and quantifying the range of seeding effects under various environmental and seeding uncertainties.

The Idaho Power Company (IPC) conducts a winter cloud-seeding program to augment snowfall in the Snake River basin for hydropower-generation purposes. The program is currently focused in two areas; the Payette River watershed and the Upper Snake River watersheds in eastern Idaho (Fig. 1). During the 2010/11 winter season, several ground-based and airborne cloud-seeding operations were conducted. From these operations, four seeding cases representing different seeding methods and various environmental conditions were selected to investigate glaciogenic cloud-seeding effects using the WRF model.

In this paper, the seeding effects and their sensitivities to model physics, environmental parameters, and cloud properties are investigated using 3D simulations of the four actual seeding events. The potential application of the coupled cloud-seeding microphysics scheme in operational programs is also demonstrated. Descriptions of four seeding cases, model configurations, and numerical experimental setups are present in section 2. Section 3 presents the results of the simulations, which is followed by a discussion of their implications in section 4. The main conclusions are summarized in section 5.

TABLE 1. Summary of the four seeding cases.

	1127_PAY	1202_PAY	1219_EID	0216_EID
Date	27 Nov 2010	2 Dec 2010	19 Dec 2010	16 Feb 2011
Seeding information				
Target	PAY	PAY	EID	EID
Method	Ground	Airborne[a]	Ground	Ground
Period (UTC)[b]	PAY 1540–2215	A4B 1502–1729	EID 2200–0500 (20), WYO 2300–0900 (20)	NEID 2300–0400 (17)
AgI (kg)[c]	1.32	3.60	7.75	1.44
Model configurations				
Period (UTC)	1500–0000 (28)	1500–1800	2200–1000 (20)	2300–0500 (17)
Radiation	Community Atmospheric Model shortwave and longwave			
PBL	MYJ scheme			
Surface	"Noah" land surface scheme			
Microphysics	Thompson scheme with AgI cloud-seeding parameterization			
Turbulence	Horizontal Smagorinsky first-order closure			
Sounding information[d]				
Time (UTC)[e]	1200	1200	2325	0108 (17)
$\overline{U}$ ($m\,s^{-1}$)	12.2	7.94	10.4	20.1
$\overline{U}$ dir (°)	161	142	205	234
N ($10^{-2}\,s^{-1}$)	1.85 (0.45)	2.33 (0.45)	1.84 (0.78)	1.51 (0.76)
Fr	0.66 (2.71)	0.34 (1.76)	0.72 (1.67)	1.66 (3.31)
Ri	1.40 (0.16)	0.71 (0.63)	0.15 (0.77)	0.02 (8.79)
P_{LCL} (hPa)	774	815	805	782
T_{LCL} (°C)	−9	0	−1	−4

[a] The altitude of the flight track is 3353 m MSL.

[b] PAY = generators over Payette, A4B = flight track A4B (red line in Fig. 1), EID = generators in the EID region (blue and green groups in Fig. 1), NEID = northern group of generators in the EID region (blue group in Fig. 1), and WYO = generators in the Wyoming Salt region (black group in Fig. 1). For EID_1219 and EID_0216, the seeding ending time and sounding time are on 20 Dec and 17 Feb, respectively, as listed in parentheses.

[c] The total mass of AgI being released into the air.

[d] Soundings are from Boise (for 1127_PAY and 1202_PAY) and Idaho Falls (for 1219_EID and 0216_EID). All parameters were calculated for the layer between the surface and 700 hPa, where AgI particles were released, except for LCL height and LCL temperature. The term $\overline{U}$ is the mean wind speed, $\overline{U}$ dir is the direction of the mean wind, N is the dry (moist in parentheses) Brunt–Väisälä frequency below (above) the LCL, $\mathrm{Fr} = \overline{U}/(NH)$ is the local bulk Froude number corresponding to dry and moist N (where H is the height of the Payette region above Boise for the 1127_PAY and 1202_PAY cases and the height of the eastern-Idaho region above Idaho Falls for the 1219_EID and 0216_EID cases), and $\mathrm{Ri} = N^2/S^2$ is the bulk Richardson number corresponding to dry and moist N, where S is the magnitude of the wind shear.

[e] Boise is a regular radiosonde station with 0000 and 1200 UTC launching time. The soundings from Idaho Falls were specifically launched for IPC seeding operations—the launching time is not the same as the regular one.

2. Experimental setups

In this study, the WRF model is run on a single domain covering most of the Snake River basin (Fig. 1). The domain consists of 420 × 200 horizontal grid points with a grid spacing of 2 km and 61 vertical terrain-following levels (as in Part I) with grid spacing varying from 20 m closest to the ground to 1400 m at the model top (Xue et al. 2010, 2012; Part I). Recent research showed that such a horizontal grid spacing ably captures wintertime precipitation patterns over complex terrain on a seasonal scale (Rasmussen et al. 2011).

The four cloud-seeding cases are 1) a ground-based seeding case over the Payette (PAY) region on 27 November 2010 (1127_PAY), 2) an airborne seeding case over the PAY region on 2 December 2010 (1202_PAY), 3) a ground-based seeding case over the region of eastern Idaho (EID) on 19 and 20 December 2010 (1219_EID), and 4) a ground-based seeding case over the EID region on 16 and 17 February 2011 (0216_EID). These cases were chosen to represent different seeding methods, seeding times, and various environmental conditions over both target areas. The details of these four seeding cases—such as seeding targets, seeding methods, seeding periods, and seeding materials being released—are listed in the first section of Table 1. The default cloud droplet number concentration was set to 100 cm^{-3} to be consistent with that parameter as used in Part I.

The model configurations are listed in the second section of Table 1. The planetary boundary layer (PBL) schemes used in this study were modified to better simulate the vertical diffusion and mixing of AgI particles. The Mellor–Yamada–Janjic (MYJ) scheme was the default PBL scheme in this study, and the Yonsei

University (YSU) scheme was tested as a component of the sensitivity experiments. For the control simulations (no simulated seeding), two sets of data were used as the initial and lateral boundary conditions to test and compare which set produced more realistic atmospheric conditions. One was the North America Regional Reanalysis (NARR) dataset with 32-km grid spacing and 3-hourly data interval, and the other was the RTFDDA WRF forecast dataset with 18-km grid spacing and an hourly interval. The RTFDDA data were taken from the archives of the outer domain of the WWMPP operational forecasts.

The observed soundings in Fig. 2 (in black) and the parameters derived from them (the last section of Table 1) show that the atmosphere was stably stratified below the lifting condensation level (LCL) and was moist through 400 hPa for each case. The stable flow was deflected by the mountain, which made the low-level wind direction align with the topography (~150° at Boise, Idaho, and ~220° at Idaho Falls, Idaho). The air above the LCL was much less stable. Consequently, the local bulk Froude numbers were greater than unity above the LCL, which implies that the AgI plumes[1] were likely to be carried over the mountain in these cases. The persistent wind shear above the LCL made the atmosphere less stable for the 1127_PAY, 1202_PAY, and 1219_EID cases (bulk Richardson numbers were small), which indicates that the AgI particles would be more easily mixed vertically than in the 0216_EID case (see section 3b for details).

One of the most important criteria for a seeding case is the cloud temperature given that AgI particles will be activated only at temperatures colder than −3°C (Meyers et al. 1995; Part I). The temperatures at the LCL were cold enough for AgI to be activated in the 1127_PAY and 0216_EID cases. The case 1202_PAY was an airborne seeding case with AgI being released at 3353 m MSL, an altitude much colder than its LCL. On the basis of the soundings from Idaho Falls, the temperature was not cold enough for AgI nucleation at the LCL in the 1219_EID case. The large areas of the eastern Idaho watersheds might not be well represented by this sounding for this particular case, however. Nonetheless, in this case the simulation showed that AgI particles reached a high-enough altitude to be activated (see section 3b for details).

Table 2 lists all of the sensitivity cases conducted in this study. The impacts of model PBL schemes, seeding rates, seeding locations, seeding timing, and cloud microphysical properties on seeding effects are investigated. A 12-h spinup simulation was performed for each case. The frequency of the model output was 30 min for most of the fields except for the vapor field, for which it was 3 h.

3. Results

a. Control cases

For limited-area mesoscale numerical weather forecasts and regional climate predictions, initial and lateral boundary conditions are needed. Good representations of such initial and lateral boundary conditions are critical for successful and reasonable simulations (Warner et al. 1997; Liang et al. 2001; Wu et al. 2005). Since this study tries to assess seeding effects under realistic conditions, two sets of available initial and lateral boundary conditions (NARR and RTFDDA) are first evaluated against observations.

Figure 2 shows the comparisons between observed soundings and those from the control simulations. The red soundings were produced from simulations driven by NARR, and blue ones were from those driven by RTFDDA. For the 1127_PAY and 1202_PAY cases, the model soundings were taken from the grid point closest to Boise at 1500 UTC (the simulation starting time) rather than at 1200 UTC when the observations were taken. Despite the time shift, both datasets generated sounding features (both the thermodynamics and the wind field) that were similar to the observed soundings above 700 hPa. The RTFDDA tended to match the observations better in the lower levels (between the surface and 700 hPa), however. For the 1219_EID and 0216_EID cases, the model soundings were taken from the grid point closest to Idaho Falls at 2330 UTC and 0100 UTC, respectively (very close to the observed sounding times). Again, both datasets agreed with observations relatively well and the RTFDDA captured low-level features better than did the NARR.

To further assess the performance of each dataset, we also compared the simulated precipitation field with observations. Figure 3 illustrates the accumulated precipitation (snow in this study) over the simulation period of each case for the NARR (Fig. 3, left panels) and RTFDDA (Fig. 3, right panels) runs. The corresponding observed snow accumulations from 153 Snowpack Telemetry (SNOTEL) sites (SNOTEL sites consist of automated measurement systems designed to collect snowpack and related climatic data in the western United States and Alaska; see details at http://www.wcc.nrcs.usda.gov/snow/) are also plotted over the model precipitation map (color-filled circles in Fig. 3). Since the instrumental resolution is 0.1 in.

[1] Most of the ground generators are located at altitudes close to or above these LCL altitudes.

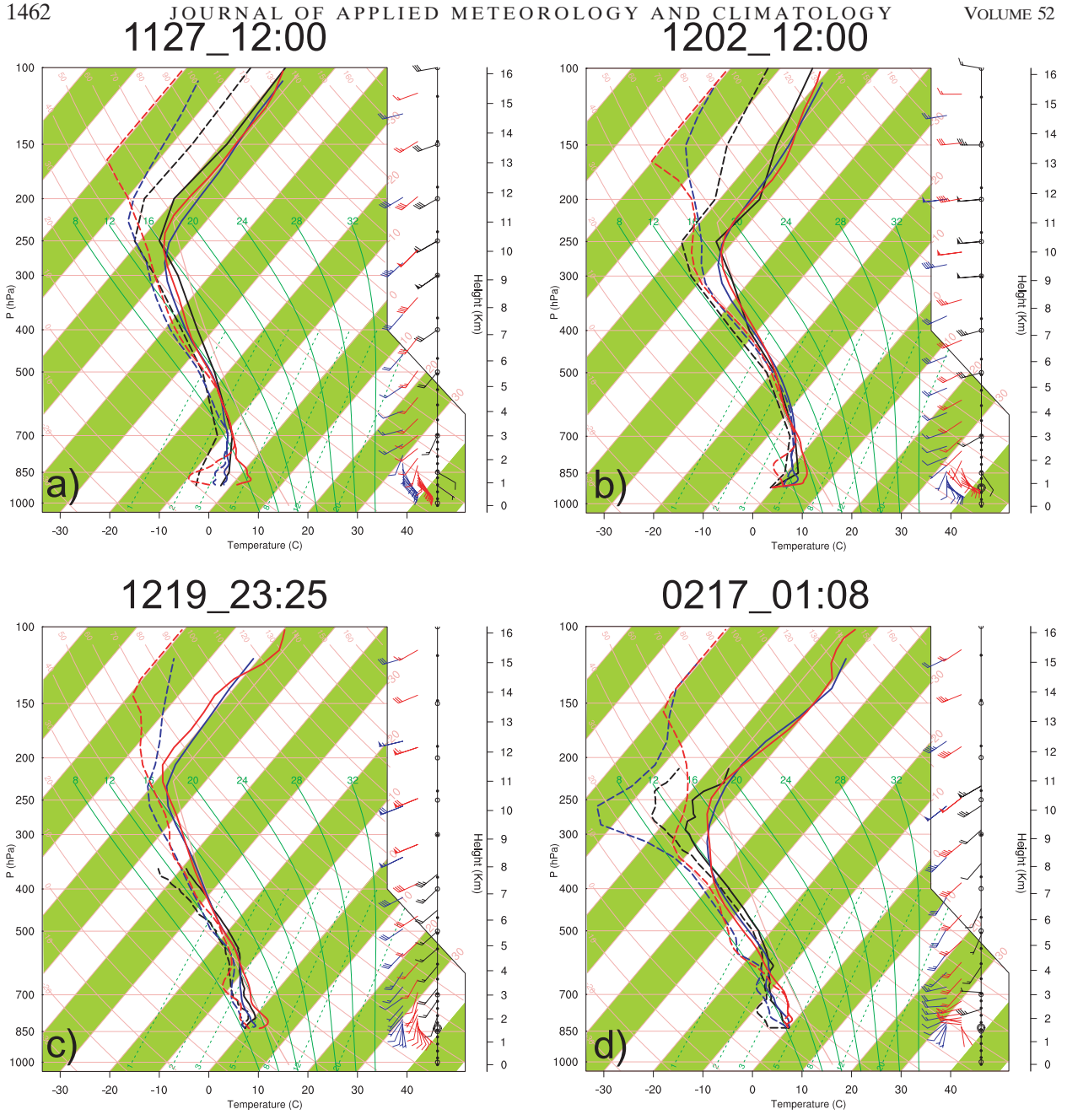

FIG. 2. Soundings of (a) 1127_PAY, (b) 1202_PAY, (c) 1219_EID, and (d) 0216_EID. The solid line is temperature, and the dashed line is dewpoint temperature. Black lines indicate observed soundings at 1200 UTC from Boise for (a) and (b) and at 2325 UTC and 0108 UTC from Idaho Falls for (c) and (d), respectively. Soundings from Boise were National Weather Service releases; those from Idaho Falls were special launches by IPC. The observed data only reached 8 and 11 km over Idaho Falls. Red and blue lines are soundings from control simulations at the closest grid points to Boise and Idaho Falls driven by the NARR and the RTFDDA, respectively. For (a) and (b), the model sounding time is 1500 UTC. For (c) and (d), the model sounding times are 2330 and 0100 UTC, respectively.

(1 in. ≈ 25.4 mm) from SNOTEL data, the accumulated precipitation is contoured with an interval of 0.1 in. as well. The color scale is the same for both model and SNOTEL precipitation.

Both the NARR and the RTFDDA results captured the precipitation over the Payette region and missed the precipitation over eastern Idaho and western Wyoming on 27 November 2010 (1127_PAY case). The RTFDDA simulation captured precipitation in northeastern Oregon and southwestern Idaho, however, whereas the NARR did not. Since 1202_PAY was the shortest case (only 3 h), the observed and simulated precipitation amounts were low. Nonetheless, the RTFDDA simulation captured precipitation over the Payette and the central

TABLE 2. Summary of sensitivity experiments. Here, "X" indicates a case was simulated and "—" means no case was simulated.

Case[a]	1127_PAY	1202_PAY	1219_EID	0216_EID
YSU	X	X	X	X
N+O	X	—	X	X
Track[b]	—	A2B	AB	AB
SR05	X	X	X	X[c]
SR2	X	X	X	X[c]
SR5	X	X	X	X[c]
E30m	X	—	—	—
L30m	X	—	—	—
IN001	X	—	—	—
IN100	X	—	—	—
CN200	X	—	—	—
CN800	X	—	—	—

[a] YSU cases used the YSU PBL scheme instead of the MYJ scheme. N+O were seeding cases with new and original generators (see Fig. 7). Track indicated whether a new or alternative flight track was used in the test. SR05, SR2, and SR5 were cases with 0.5, 2, and 5 times the original seeding rates, respectively. E30m and L30m were cases in which seeding occurred 30 min earlier and later than the original starting time, respectively. IN001 and IN100 were cases with 1% of and 100 times the background IN concentrations, respectively. CN200 and CN800 were cases with cloud droplet concentrations of 200 and 800 cm^{-3}, respectively.

[b] For the 1202_PAY case, A2B was tested instead of A4B. For the 1219_EID and 0216_EID cases, the northern group of ground generators was replaced by an imaginary flight track (see Fig. 7).

[c] The 0216_EID seeding-rate cases were tested for the airborne-seeding scenario.

Idaho regions better than did the NARR simulation. For the longest case (1219_EID), accumulated precipitation amounts were high for both observed and model results. The NARR run missed the whole precipitation pattern over eastern Idaho and western Wyoming, whereas the RTFDDA run reasonably simulated the observed pattern in this region. On 16 February 2011 (0216_EID case), both the NARR and the RTFDDA runs generated precipitation over northwestern and western Wyoming that was not observed at the SNOTEL sites. The RTFDDA run simulated the precipitation over southeastern Idaho and southwestern Wyoming regions while the NARR run did not.

The comparisons of soundings and accumulated precipitation between control simulations and observations indicate that the RTFDDA WRF forecast data generated more realistic results than did the NARR data. Additional comparisons between observed liquid water path (LWP) from radiometers and model-simulated LWP also confirmed the better performance of the RTFDDA data (not shown).[2] On the basis of these results, we performed seeding and sensitivity simulations using the RTFDDA data as the initial and lateral boundary conditions.

b. Seeding cases

As described in Part I, the AgI cloud-seeding parameterization prescribes AgI sources in the model at fixed grid points or changing positions over specified time periods. Thus, the actual seeding periods and seeding rates listed in Table 1 were simulated for all cases.

Figure 4 shows the plan views of AgI number concentration (m^{-3}), LWP (mm), and precipitation difference (mm) between seeding and control simulations for all four cases. The four panels in the left column illustrate the instantaneous AgI number concentrations in logarithmic scale at 3000 m MSL (color shaded), which is a representative altitude for seeding conditions (see Fig. 5), and regions with an ice saturation ratio of greater than 1.04 (red outlines) in the midtime of the simulations (1930 UTC for 1127_PAY, 1630 UTC for 1202_PAY, 0400 UTC for 1219_EID, and 0200 UTC for 0216_EID). In general, AgI plumes were advected downwind of the prevailing wind direction. The horizontal spread of the plume was associated with the wind shear and the atmospheric stability. The vertical spread of the plume was mainly a function of the atmospheric stability and the vertical motions associated with the complex terrain, which were not presented in the idealized 2D simulations (Part I). As listed in Table 1, the Ri value above the LCL of the 0216_EID case was much greater than the others, which indicated less-efficient dispersion of AgI particles vertically in this case. This is evident in Figs. 4a1–4a4 and Fig. 5. AgI number concentration of the airborne seeding case was higher than for the ground-based seeding cases at this level because the airborne-seeding altitude is 3353 m MSL and the average altitude of generators is about 1800 m MSL over the Payette region and eastern Idaho.

The parameterizations of AgI ice-nucleating ability in the coupled scheme require water supersaturation (a subset of red-outlined regions) and ice saturation ratio greater than 1.04 for condensation-freezing mode, deposition mode, and contact-freezing mode to be active (Part I; Meyers et al. 1995). Therefore, ice nucleations are expected in the overlapping areas between AgI plumes and red-outlined regions. The cellular feature of ice-supersaturated areas was determined mainly by the vertical motions induced by the complex terrain. From the finding in Part I that the local AgI activation ratio is between 0.02% and 2% under most seeding conditions, an AgI number concentration of $10^5\ m^{-3}$ ($100\ L^{-1}$) or higher is needed to provide significantly more ice nuclei than the background value. The average

[2] Good-quality radiometer data for the 0216_EID case were only available in Afton, Wyoming.

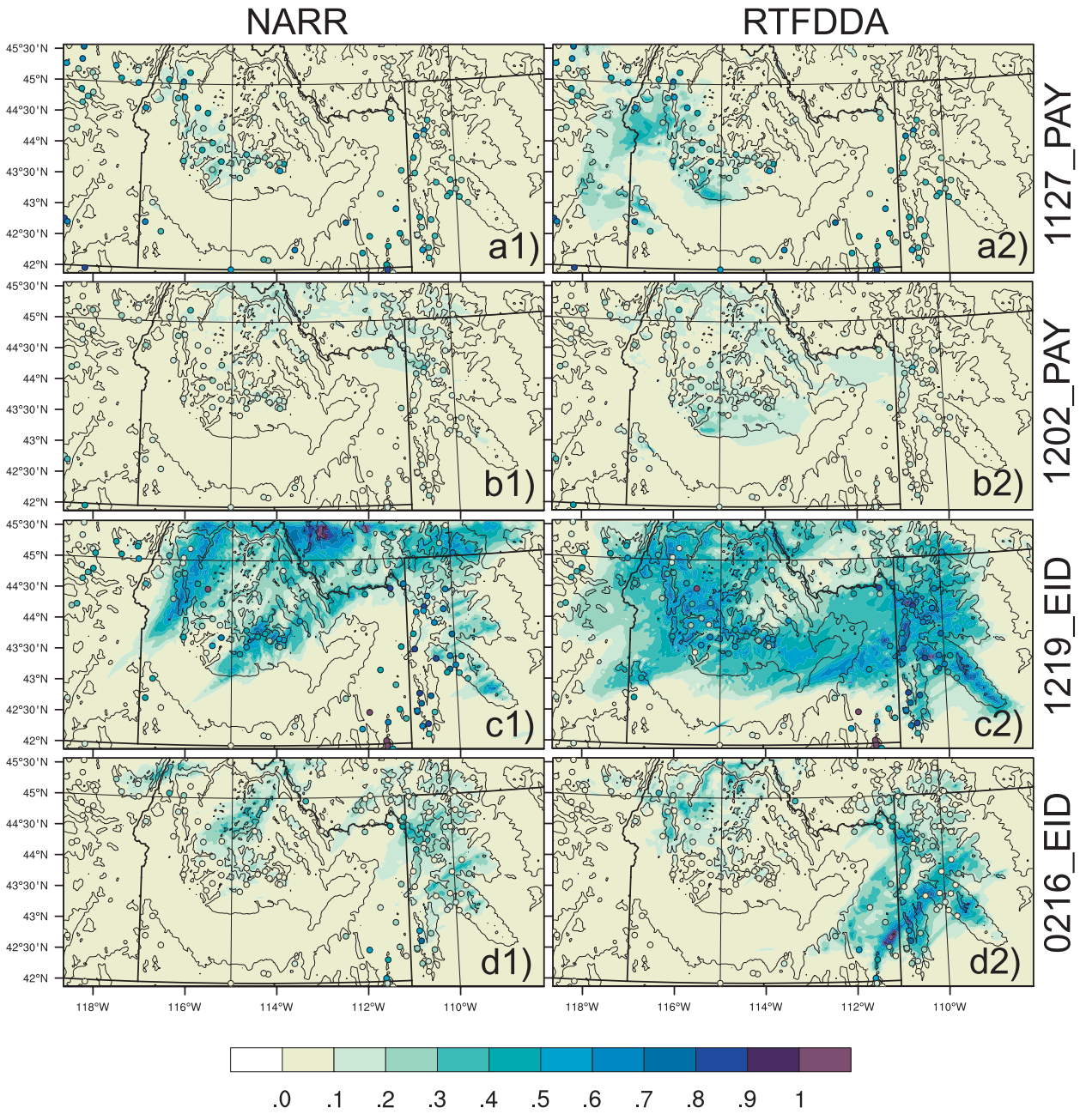

FIG. 3. Accumulated precipitation (in.) of control simulations and SNOTEL sites for (a1),(a2) 1127_PAY, (b1),(b2) 1202_PAY, (c1),(c2) 1219_EID, and (d1),(d2) 0216_EID for (left) NARR and (right) RTFDDA results. Model precipitation is color shaded, overlaid by SNOTEL precipitation in color-filled circles. The color scale is the same for both model and SNOTEL precipitation. The terrain height is shown by the thin black contours, starting at 500 m with an interval of 1000 m.

ice crystal number concentration of the seeded clouds was found to range between 25 and 100 L^{-1} for the ground-based seeding cases and ~150 L^{-1} for the airborne-seeding case (not shown). These simulated ice concentrations were in good agreement with previous studies (Deshler et al. 1990; Meyers et al. 1995; Reisin et al. 1996; Geerts et al. 2010).

Figures 4b1–4b4 show the LWP[3] of the control simulations (color shaded) and regions of AgI number concentration of greater than 10^5 m^{-3} at 3000 m MSL

[3] It is the supercooled LWP since the temperatures at the LCL were below 0°C in all cases (see Table 1).

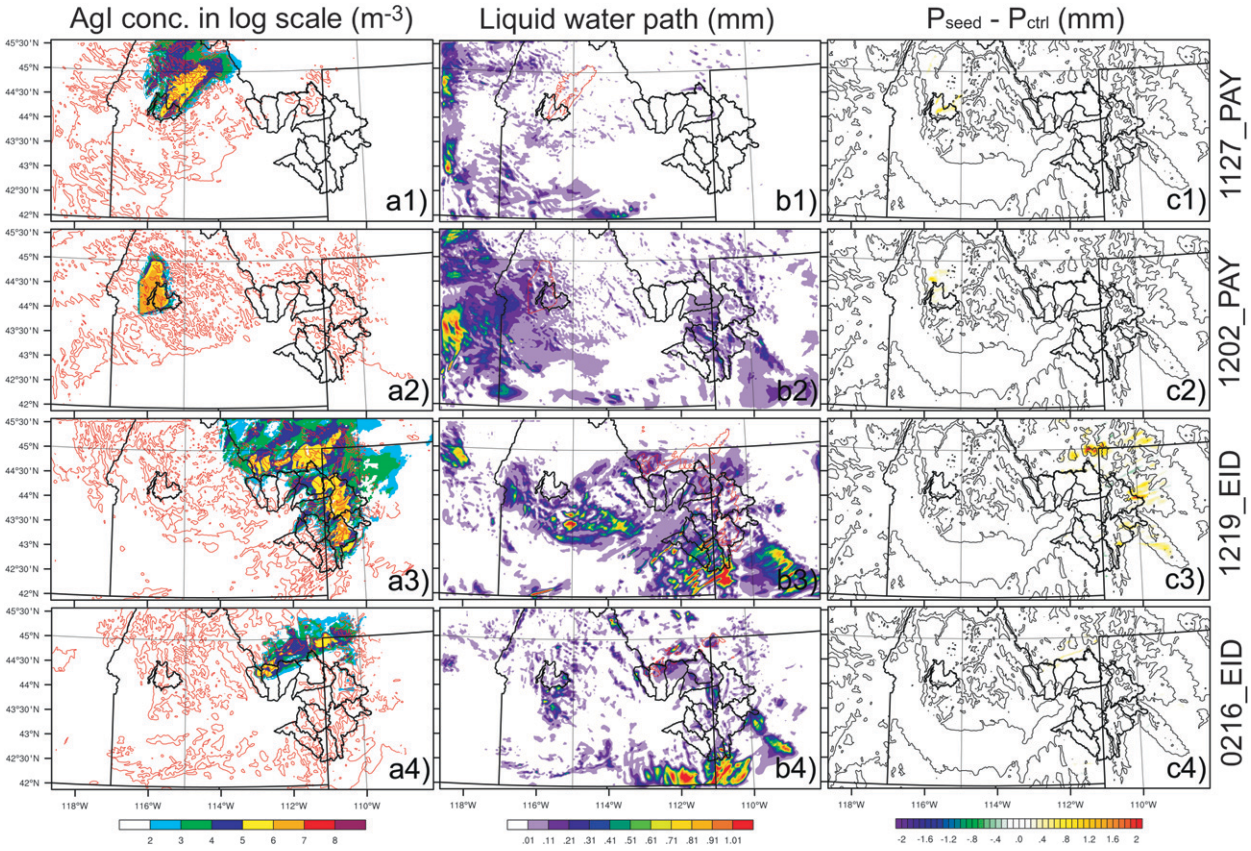

FIG. 4. Plan views of (a1)–(4) AgI number concentration (m^{-3}) at 3000 m MSL in logarithmic scale and regions with ice saturation ratio greater than 1.04 (red outlines) in the midtime of the simulations (1930 UTC for 1127_PAY, 1630 UTC for 1202_PAY, 0400 UTC for 1219_EID, and 0200 UTC for 0216_EID), (b1)–(b4) liquid water path (mm) and regions of AgI concentration greater than $10^5\,m^{-3}$ at 3000 m MSL (red outlines) at the same times as in (a), and (c1)–(c4) precipitation differences (mm) between the seeding runs and the control runs at the end of the simulations for all cases. The terrain height is shown by the thin black contours, starting at 500 m with an interval of 1000 m. The watersheds are indicated by thick black lines.

(red outlines) at the same times as in Figs. 4a1–4a4. The coexistence of supercooled liquid water and ice nuclei facilitated the growth of AgI-nucleated ice crystals through both the Bergeron–Findeisen process and the riming process. Supercooled liquid water drops can scavenge AgI particles and subsequently are frozen through contact freezing and immersion freezing of AgI. At these times, the 1202_PAY and 1219_EID cases appeared to have faster snow growth rates than the other two cases because of more liquid water content around the AgI plumes. The liquid water field was constantly changing, however, which might help the AgI-nucleated crystals to grow at other times in the 1127_PAY and 0216_EID cases. The very high concentration of AgI inside cloud droplets as a result of the model artifact in 2D simulations was not observed in these 3D simulations. The magnitude of AgI concentration in cloud droplets was two orders of magnitude smaller in real cases because of efficient dispersion and turbulent mixing (not shown). Consequently, the nucleation rate of immersion freezing was considerably reduced relative to 2D simulations.

The precipitation differences between the seeding runs and the control runs at the end of the simulations are plotted in Figs. 4c1–4c4 for all cases. For the 1127_PAY case, the simulated precipitation enhancements were mainly within the Payette target area with some downwind signals, which was different from the 2D result that ground-based seeding mainly enhanced downwind precipitation. This result was partly due to the weak low-level wind speed[4] and partly due to the real topography and three-dimensional domain used in this study. The precipitation enhancements were very localized and

[4] Averaged wind speed below 500 m AGL was ~7 $m\,s^{-1}$ in this case, whereas it was ~15 $m\,s^{-1}$ in the 1219_EID and 0216_EID cases.

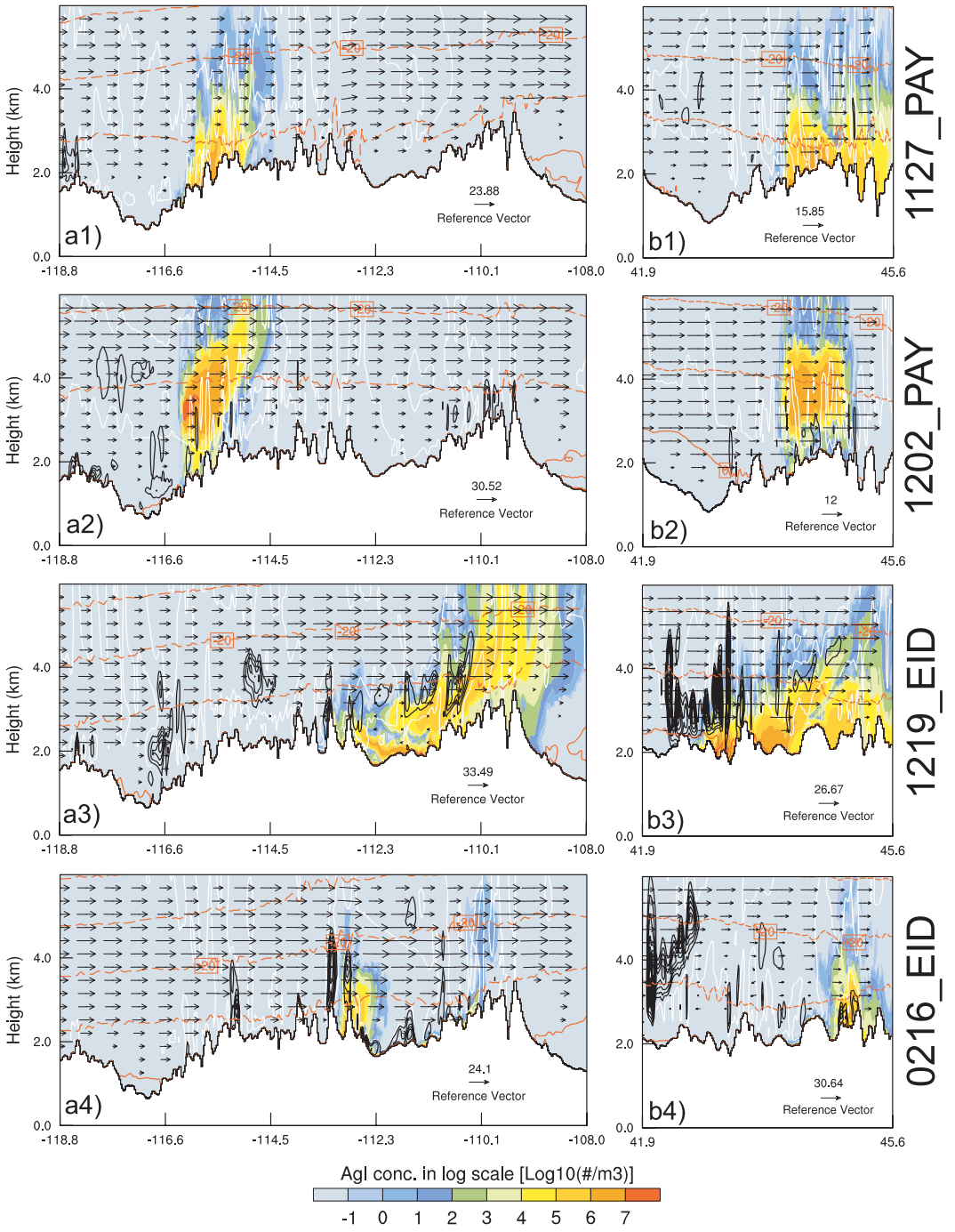

FIG. 5. (left) West–east and (right) south–north cross sections below 6 km at the same times as in Figs. 4a(1)–(4) of (a1),(b1) 1127_PAY, (a2),(b2) 1202_PAY, (a3),(b3) 1219_EID, and (a4),(b4) 0216_EID. AgI number concentration (m^{-3}) is color shaded on a logarithmic scale. Cloud water mixing ratios ($g\,kg^{-1}$) are black contoured, with an interval of $0.1\,g\,kg^{-1}$. Wind fields ($m\,s^{-1}$) are indicated by vectors. Temperatures (°C) are red contours, with an interval of 10 °C. White lines indicate regions with ice saturation ratio greater than 1.04.

were generally in the upwind region in the 1202_PAY case. Most of the seeding signals were in the downwind regions of the eastern-Idaho target area in the 1219_EID case. These effects were associated with strong low-level wind and the high-altitude terrain over these areas. The negative signals in this case were attributed to microphysical and dynamic feedbacks on the spatiotemporal patterns of the cloud formation and the precipitation

onset introduced by the seeding materials. The weakest seeding effect was observed in the 0216_EID case in which almost all of the precipitation enhancements occurred downwind of the target area.

The spillover ratio was well defined in the 2D simulation with uniform wind direction, unique mountain peak, and one-dimensional continuous distribution of precipitation. It is not well defined under realistic conditions, however. In 3D simulations, the wind field was not steady, the topography was much more complicated than the 2D idealized mountain (multiple ridges and different summit heights), and the spatial distribution of precipitation was not continuous. Therefore, systematic and quantitative examinations of spillover ratio in 3D simulations are difficult. Nonetheless, the upwind seeding effect of the 1202_PAY case and the downwind seeding signals in the 1219_EID and 0216_EID cases agreed with the finding in 2D simulations qualitatively well. In general, seeding increased precipitation in all cases, with some locations having negative effects. The agreement between areas with seeding signal and collocation of supercooled liquid water and seeding materials in this study was simulated by Meyers et al. (1995) as well (see Figs. 4b1–4b4 and 4c1–4c4).

More details on how seeding affects the wintertime orographic precipitating clouds can be seen in the vertical cross sections of these cases. Figure 5 shows the west–east cross sections (Fig. 5, left panels) and south–north cross sections (Fig. 5, right panels), below 6 km, of AgI number concentration (m^{-3}) on a logarithmic scale (color shaded), cloud water mixing ratio (black contours; $g\,kg^{-1}$), wind (vectors; $m\,s^{-1}$), temperature (red contours; °C), and regions with ice saturation ratio of greater than 1.04 (white outlines) at the same times as in Figs. 4a1–4a4 and 4b1–4b4 for all cases. The west–east cross section is indicated by the horizontal yellow dashed line in Fig. 1. The south–north cross section of 1127_PAY and 1202_PAY is represented by the perpendicular yellow dashed line on the left, and the line on the right is for 1219_EID and 0216_EID (see Fig. 1).

AgI plumes from ground generators reached an altitude of 2 km above ground with significant concentration ($>10^5\,m^{-3}$) when the meteorological conditions were favorable (high wind shear and low Ri number in the 1127_PAY and 1219_EID cases). Under unfavorable conditions such as in the 0216_EID case (little wind shear and high Ri number), the AgI plume was suppressed below 1 km above ground. As discussed in previous paragraphs, the cellular feature of high ice-supersaturated regions caused by the complex terrain was also illustrated in Fig. 5. Such vertical motions were responsible for transportation of highly concentrated AgI into high altitudes as well, which was not observed in 2D simulations (Part I). The broader ice-supersaturated area than the liquid water region as found in 2D simulations (Part I) was also evident in 3D simulations. From the findings in Part I, the optimum AgI-nucleating condition can be defined as the collocation of high concentration of AgI particles ($>10^5\,m^{-3}$), temperature between −20° and −8°C, high ice supersaturation ($S_i > 1.04$) and nonnegligible supercooled liquid water content. All four cases met most of these criteria (as shown in Fig. 5). Therefore, positive seeding effects are expected in these cases.

The analyses in Figs. 4 and 5 showed how seeding affected precipitation in a spatial sense. Figure 6 illustrates the time series of the total mass differences of water vapor (circles), liquid water in the air (short-dashed lines), solid-phase water in the air (long-dashed lines), and precipitation on the ground (solid lines) between seeding and control simulations for all cases over the entire domain. Since the output frequency of the water vapor field is 3 h, they are plotted as discrete symbols on each panel. Note that the detailed microphysical processes need huge storage space for these 3D simulations, which was unavailable to this study. Thus, detailed microphysics analyses as done in Part I were not performed in this paper.

It is found that the seeding materials did not affect the cloud or the precipitation right after they were released from the generators or the aircraft. It took 2–3 h for ground-based seeding and less than 1 h for airborne seeding to notably affect the cloud and the precipitation, which confirmed the findings in Deshler et al. (1990). This is reasonable given the time needed for AgI particles to be transported and dispersed into optimum nucleation regions. The changes of liquid water/vapor and those of solid water/precipitation were generally in counterphase because seeding materials converted liquid water and vapor into ice particles, which grew at the expense of vapor and liquid water. It is worth mentioning that the sum of these terms at a certain moment after seeding started is not necessarily equal to zero because the fluxes of these variables through the lateral boundaries of the domain were modified by the seeding process, especially for long-time runs and EID simulations.[5]

An interesting phenomenon presented here is that the impacts of seeding materials on clouds occurred earlier than the impacts on the precipitation in the 1202_PAY and 1219_EID cases, whereas it was the opposite for the 1127_PAY and 0216_EID cases. For the 1127_PAY and 0216_EID cases, highly concentrated AgI particles

[5] In these simulations, impacts of seeding materials on vapor, liquid, and ice were advected out of the boundaries within the simulation time.

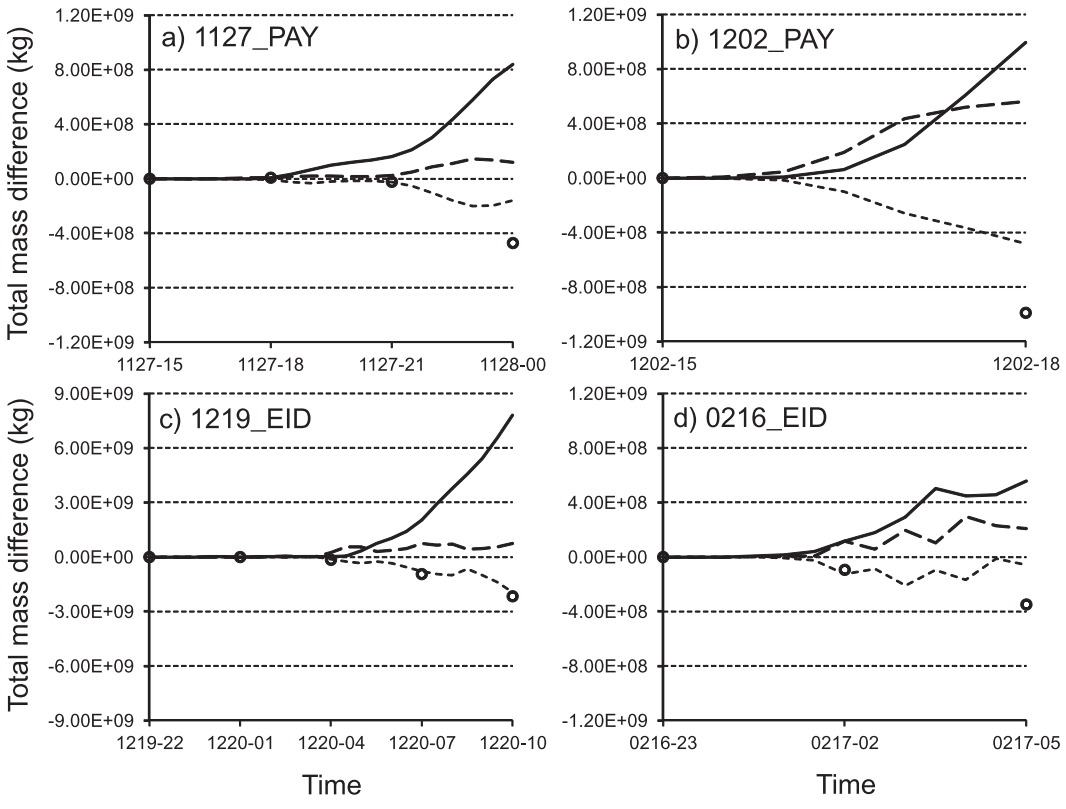

FIG. 6. Time series of the total mass differences (kg) of water vapor (circles), liquid water in the air (short-dashed lines), solid-phase water in the air (long-dashed lines), and precipitation on the ground (solid lines) between seeding and control runs over the entire domain for (a) 1127_PAY, (b) 1202_PAY, (c) 1219_EID, and (d) 0216_EID.

entered the region with high ice supersaturation that were very close to the ground before they encountered liquid water contents. Deposition nucleation was the only active mode. Diffusional growth and aggregation of these newly nucleated ice crystals were the main growth mechanisms in this case. Hence, these close-to-ground crystals fell on the ground as precipitation quickly. On the other hand, in 1202_PAY and 1219_EID, high concentrations of AgI particles quickly reached high altitudes where both liquid water contents and high ice supersaturation coexisted. Therefore, liquid water was consumed and ice-phase water was increased by AgI particles before they reached the ground as precipitation. In all cases, more vapor was depleted than liquid water by seeding, which agreed with the finding in Part I that more enhanced snow came from deposition growth than from riming.

Overall, the 3D simulations of actual seeding events agreed qualitatively well with the 2D idealized results in Part I, such as AgI particles nucleating ice crystals through different modes under various conditions, AgI-nucleated ice crystals growing by diffusion and riming and reaching the ground as snow, and ground-based seeding increasing precipitation on the lee side of the mountain most of time. Because of the stronger dispersion and turbulent mixing of AgI particles as the result of complex topography and the extra dimension used in these simulations, immersion freezing was not as active as in Part I and ground-based seeding enhanced upwind precipitation under low wind conditions.

c. *Sensitivity tests*

The sensitivities of seeding effects to model PBL schemes, seeding method, rate, location and timing, and cloud microphysical properties in a 3D setup are investigated in this section (see Table 2). For each ground-based seeding case, a test of adding five automatic generators was performed (N+O). An airborne test included replacing the original A4B track in 1202_PAY with the A2B track. For the 1219_EID and 0216_EID cases, the northern group of generators (blue group in Fig. 1) was replaced by airborne seeding from the track AB. Note that the seeding-rate tests of the 0216_EID case were based on the airborne scenario. Figure 7 shows the new generator locations (blue circles) and the alternative flight tracks (red segments).

The precipitation enhancements by seeding of default seeding cases (BASE) and all of the sensitivity

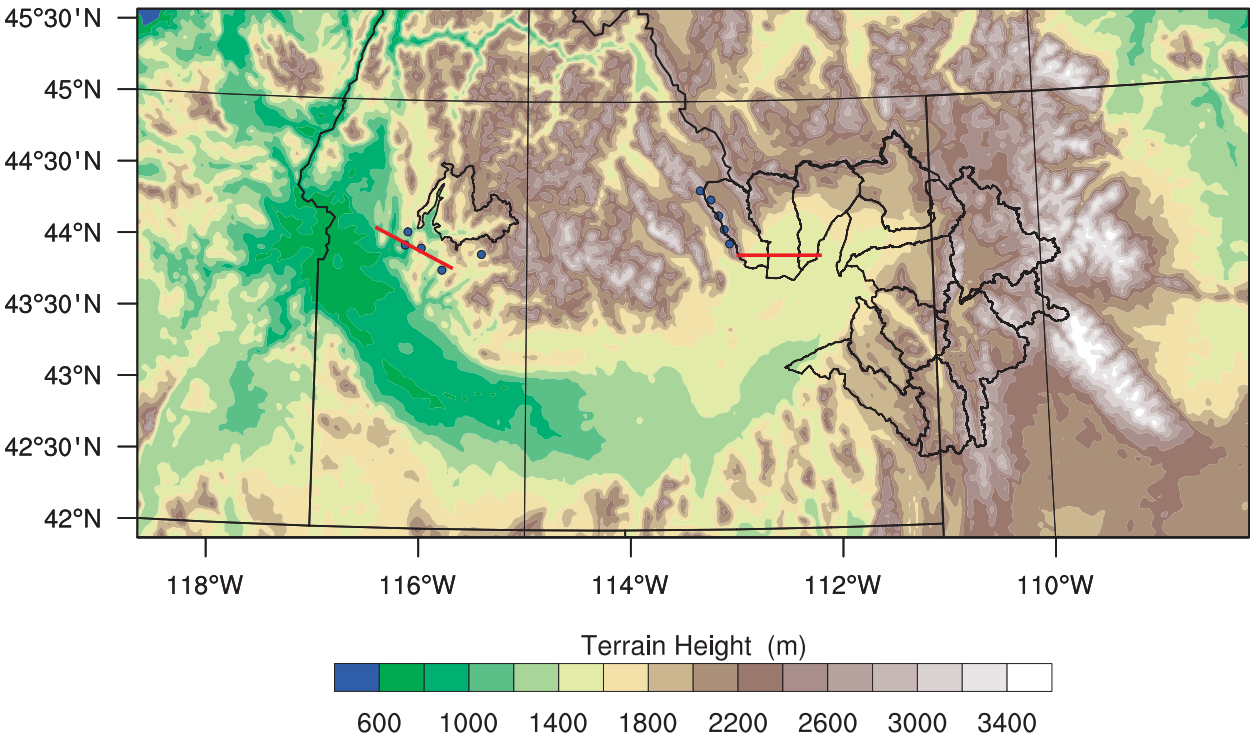

FIG. 7. As in Fig. 1, but for new generator locations indicated by blue circles, the flight track A2B indicated by the red segment close to the Payette region, and the flight track AB indicated by the red segment over northeastern Idaho.

experiments (see Table 2) are listed in Table 3. The absolute amount of precipitation enhancement is listed in the unit of acre feet (1 acre ft $\approx$ 1233.5 m^3 $\approx$ 1.233 $\times$ 10^6 L), which is commonly used in the hydrology community. The relative increase of precipitation by seeding is also listed in percentage. Both absolute amounts and relative increases were calculated within the entire domain, within the Snake River basin, and within the target areas.

It is found that seeding increased precipitation over the entire domain, the basin, and target areas in all of the sensitivity cases. The relative increases of precipitation were small over all of the regions in all cases (<5%), however. The absolute amounts of precipitation enhancements over the basin or target areas were small portions of those over the entire domain (<50%). The portions were much higher in the 1127_PAY and 1202_PAY cases relative to the 1219_EID and 0216_EID cases. The topographic features (mountain height, half-width, and complexity), flow patterns associated with the topography, and meteorological conditions might cause such differences between the Payette region and the region of eastern Idaho.

Such differences are also manifested by the sensitivity simulations using the YSU PBL scheme. The YSU and the MYJ PBL schemes simulated very similar seeding effects over the Payette region (1127_PAY and 1202_PAY cases) whereas the YSU run simulated less than 50% of the effects of the MYJ simulations over the region of eastern Idaho (1219_EID and 0216_EID). The treatment of PBL directly affects the vertical diffusion of AgI particles. The less-pronounced seeding effects of the YSU simulations could be attributed to the fact that the YSU scheme simulated a more stable boundary layer than does the MYJ run and lifted fewer AgI particles into the optimum seeding region. The investigation of why the YSU PBL scheme simulated very different boundary layer features when compared with the MYJ scheme over the region of eastern Idaho is beyond the scope of this paper and is subject to another study.

The purpose of testing the new and original locations of ground generators (N+O) is to find out, by focusing on the seeding effects over the target area, whether these new locations can improve targeting. This can be assessed by analyzing the results of N+O tests and the seeding-rate tests (SR05, SR2, and SR5). Figure 8 shows the relations between seeding-rate ratio and normalized seeding effect (precipitation enhancement normalized by that of BASE case) over the domain for all cases and those over the target areas for the 1127_PAY and 1219_EID cases. Similar to what has been found in the 2D sensitivity tests (Part I), such relations in 3D simulations showed that they followed the power law and that the slopes were steeper for ground-based seeding

TABLE 3. Simulated precipitation changes due to seeding for the sensitivity experiments (af = acre ft).

Case	Domain (af)	Domain (%)	Basin (af)	Basin (%)	Target (af)	Target (%)
			1127_PAY			
BASE	682	0.24	281	0.12	282	2.06
YSU	614	0.21	293	0.13	273	1.96
N+O	807	0.28	384	0.17	341	2.49
SR05	448	0.16	175	0.08	178	1.30
SR2	977	0.34	416	0.18	421	3.07
SR5	1463	0.51	651	0.28	652	4.75
E30m	705	0.25	267	0.12	306	2.23
L30m	635	0.22	274	0.12	257	1.87
IN001	713	0.25	288	0.13	289	2.11
IN100	523	0.18	205	0.09	235	1.70
CN200	737	0.26	324	0.14	311	2.27
CN800	900	0.32	446	0.20	389	2.85
			1202_PAY			
BASE	805	0.29	385	0.22	392	2.89
YSU	836	0.30	376	0.22	399	2.91
A2B	425	0.16	305	0.18	206	1.52
SR05	611	0.22	273	0.16	290	2.14
SR2	1002	0.37	493	0.29	494	3.64
SR5	1257	0.46	625	0.36	606	4.47
			1219_EID			
BASE	6330	0.41	1023	0.11	1044	0.39
YSU	2674	0.17	241	0.03	239	0.09
N+O	6935	0.44	1219	0.14	1098	0.41
AB	4961	0.32	1051	0.12	992	0.37
SR05	4335	0.28	850	0.09	796	0.30
SR2	9388	0.60	1855	0.21	1742	0.65
SR5	13 481	0.86	2630	0.29	2477	0.92
			0216_EID			
BASE	451	0.08	64	0.02	68	0.04
YSU	217	0.04	8	0.00	12	0.01
N+O	544	0.10	83	0.03	106	0.06
AB	544	0.10	209	0.08	201	0.11
ABSR05	366	0.06	149	0.05	140	0.08
ABSR2	698	0.12	249	0.09	256	0.15
ABSR5	932	0.17	318	0.11	321	0.18

cases relative to airborne seeding cases.[6] The filled symbols in Figs. 8a, 8c, 8e, and 8f indicate the corresponding results of N+O cases. The data points of the N+O cases in Figs. 8e and 8f lay either on or below the regression line defined by the seeding-rate tests, which indicated that no apparent improvements of targeting by these new generators were achieved.

The alternative flight-track tests for 1202_PAY, 1219_EID, and 0216_EID were conducted to investigate the targeting issue as well. As seen from Table 3, the original track A4B performed much better than the track A2B being tested for the 1202_PAY case mainly because of the orientation of the track A4B that captured the optimum seeding region to the north of the Payette watershed. The flight track AB was designed to replace the northern group of generators in the region of eastern Idaho (blue generators in Fig. 1), which was identified to have consistent targeting problems (not shown). In the 1219_EID case, the airborne seeding lasted from 2300 UTC 19 December to 0200 UTC 20 December. The AgI being released was 4.32 kg as compared with the 2.02 kg that was released by the northern-group generators. With more AgI being released, the seeding effect over the target area was still less than the ground-based seeding scenario, which implied track AB is not a good alternate for this group in this case, mainly because of unfavorable atmospheric conditions. In the 0216_EID case, AB seeding also covered 3 h from 0000 to 0300 UTC on 17 February. The AgI amount from generators was 1.44 kg in this case. Unlike the 1219_EID case, with 2 times as much AgI materials, the AB seeding almost tripled the precipitation over the target area and the Snake River basin in

[6] The seeding-rate tests of 0216_EID were for an airborne seeding scenario. So, there is no comparison between N+O and these seeding-rate results.

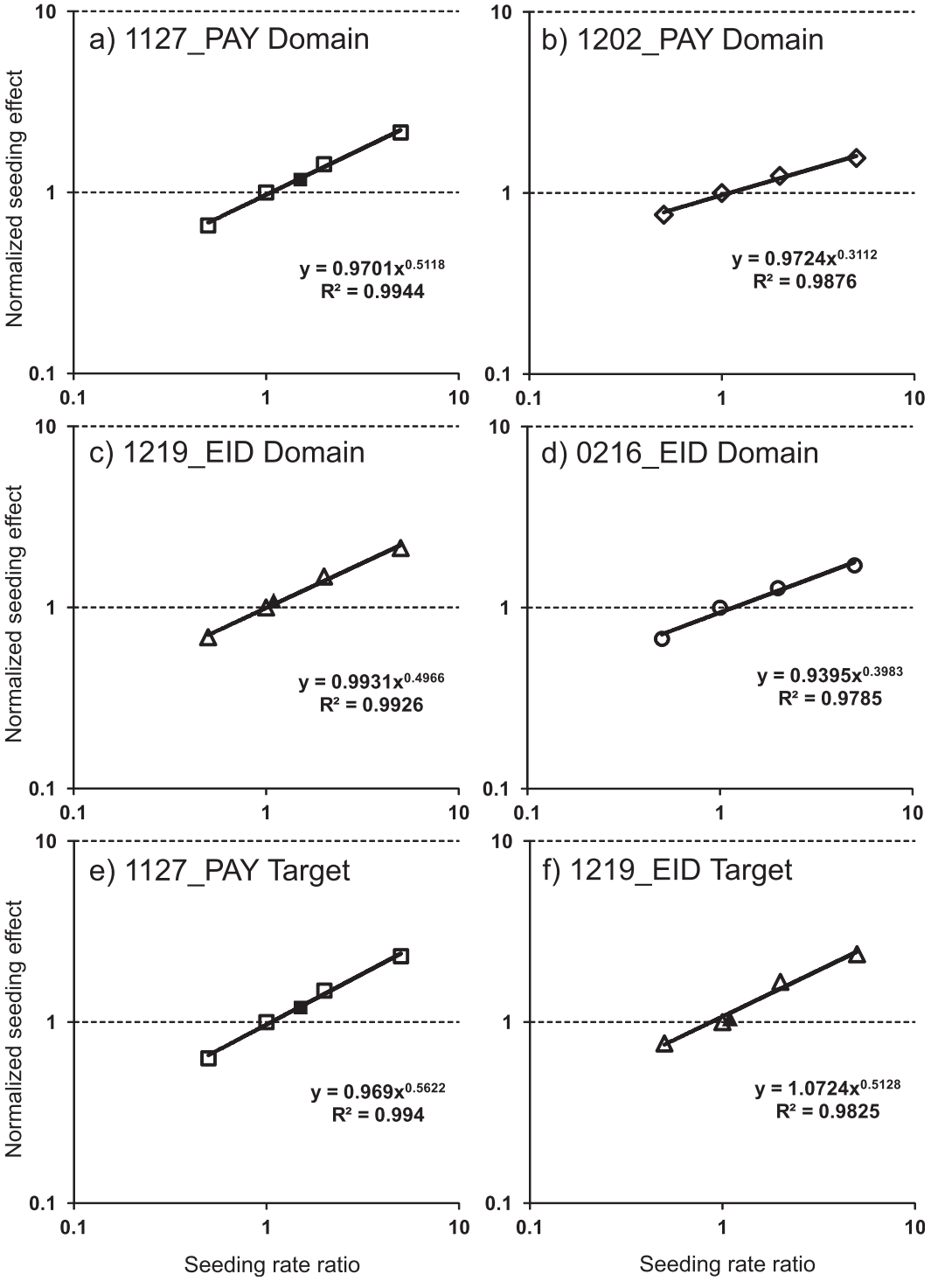

FIG. 8. Scatterplots of the normalized seeding effect as a function of seeding-rate ratio over the entire domain for (a) 1127_PAY, (b) 1202_PAY, (c) 1219_EID, and (d) 0216_EID. Also shown is the same relation over the target region for (e) 1127_PAY and (f) 0216_EID. The filled symbols in (a),(c),(e), and (f) indicate the data points of N+O.

this case. As described by the power law, tripling the default seeding rate cannot achieve triple seeding effect from ground-based seeding. Thus, the targeting was improved by switching ground-based seeding to airborne seeding in the 0216_EID case, which echoed the finding in Part I that airborne seeding is more effective than ground-based seeding because of the improved targeting of the AgI to optimum cloud regions for snow growth and fallout. The seeding effect over the entire domain from AB seeding was just 21% higher than the ground-based seeding, however. These airborne tests implied that airborne seeding is generally more efficient than ground-based seeding in terms of targeting but that its efficiency depends on meteorological conditions near the target areas.

Limited by the computing resources, we only performed sensitivity tests of seeding timing and cloud microphysical properties for the 1127_PAY case. The results showed that just by shifting the seeding starting time 30 min before or after the original time a 20% difference of seeding effect was achieved in the target area. This result poses a strong requirement for an accurate forecast and prompt decision making on seeding timing in seeding operations. The tests of different background ice nuclei (IN) concentrations and cloud droplet concentrations led to the same conclusion as the 2D sensitivity tests (Part I) did that, the less efficient the natural precipitation processes are, the more precipitation enhancements will result by seeding (IN001 and CN800 cases), and vice versa (IN100 and BASE cases). Givati and Rosenfeld (2005) argued that cloud seeding might compensate the precipitation loss due to anthropogenic pollution. In our simulations, seeding did make up the precipitation loss in the CN200 case but could not offset the loss in the CN900 case.[7] Therefore, the suppression of precipitation by heavy pollution tends to be stronger than the precipitation invigoration by the glaciogenic orographic cloud seeding.

One of the major goals of collecting so many sensitivity results is to find out the range of seeding effects under various conditions for a certain seeding event. The normalized seeding effects over the entire domain, the Snake River basin, and the target areas of all of the sensitivity experiments are plotted in the left panels in Fig. 9. The right panels in Fig. 9 are cases without seeding-rate tests, which are more representative for this assessment. It is found that the seeding effects in the basin and the target (Fig. 9, middle and bottom panels) were more scattered than those in the domain (Fig. 9, top panels). Again, this implied the uncertainty and importance of targeting. When the data points of seeding-rate tests were removed, the normalized seeding effects were confined between 0.4 and 1.4 over the entire domain. The circles on the top in Figs. 9b2 and 9c2 represented the AB test in 0216_EID, which was not consistent with the original ground-based seeding scenario. The circles and triangles at the bottom in Figs. 9b2 and Figs. 9c2 were the YSU cases, which need further investigation. If these outliers were to be removed, the normalized seeding effects in the basin and the target would be in the range between 0.5 and 1.6. Therefore we tentatively conclude from this sensitivity study that the normalized seeding effects are from 0.4 to 1.6 under various conditions for a certain case.

4. Discussion

In section 3a, the accumulated precipitation of SNOTEL sites was compared with that of model simulations. Comparisons of precipitation time series with daily interval between individual SNOTEL sites and WRF simulations were presented in Rasmussen et al. (2011). It was shown that, at grid spacing of 6 km or finer, WRF simulations with the Thompson microphysics scheme captured the observed precipitation trend very well within an error of 20% over the entire Colorado headwater region in many winter seasons. Similar analyses have been performed over the Sierra Madre and the Medicine Bow Mountains (target areas of WWMPP) in March of 2008 (K. Ikeda 2012, personal communication). The results showed good agreement between RTFDDA-WRF forecasts and SNOTEL data as well (not shown). Such analyses are hard to repeat in this study because of the short simulation periods (subdaily) and coarse temporal resolution of SNOTEL measurements (hourly or 3 hourly depending on sites). The few data points in the time series imposed great uncertainties such as instrument errors and spatial–temporal errors of simulated precipitation patterns.

The better control results of RTFDDA runs could be partly attributed to the fact that the RTFDDA forecast data have a finer grid spacing and time interval than does the NARR dataset (18 vs 32 km, and hourly vs 3 hourly). The larger number of observations in higher resolutions (both temporal and spatial) being assimilated into the RTFDDA-WRF system that are not available to the NARR data contribute to the better performance of RTFDDA simulations as well.[8] Another noticeable

[7] A similar result was found in the 2D ground-based seeding simulations in Part I.

[8] The observations of the Wyoming Department of Transportation Road Weather Information System and special launched radiosondes in Saratoga, Wyoming, were assimilated by the RTFDDA system.

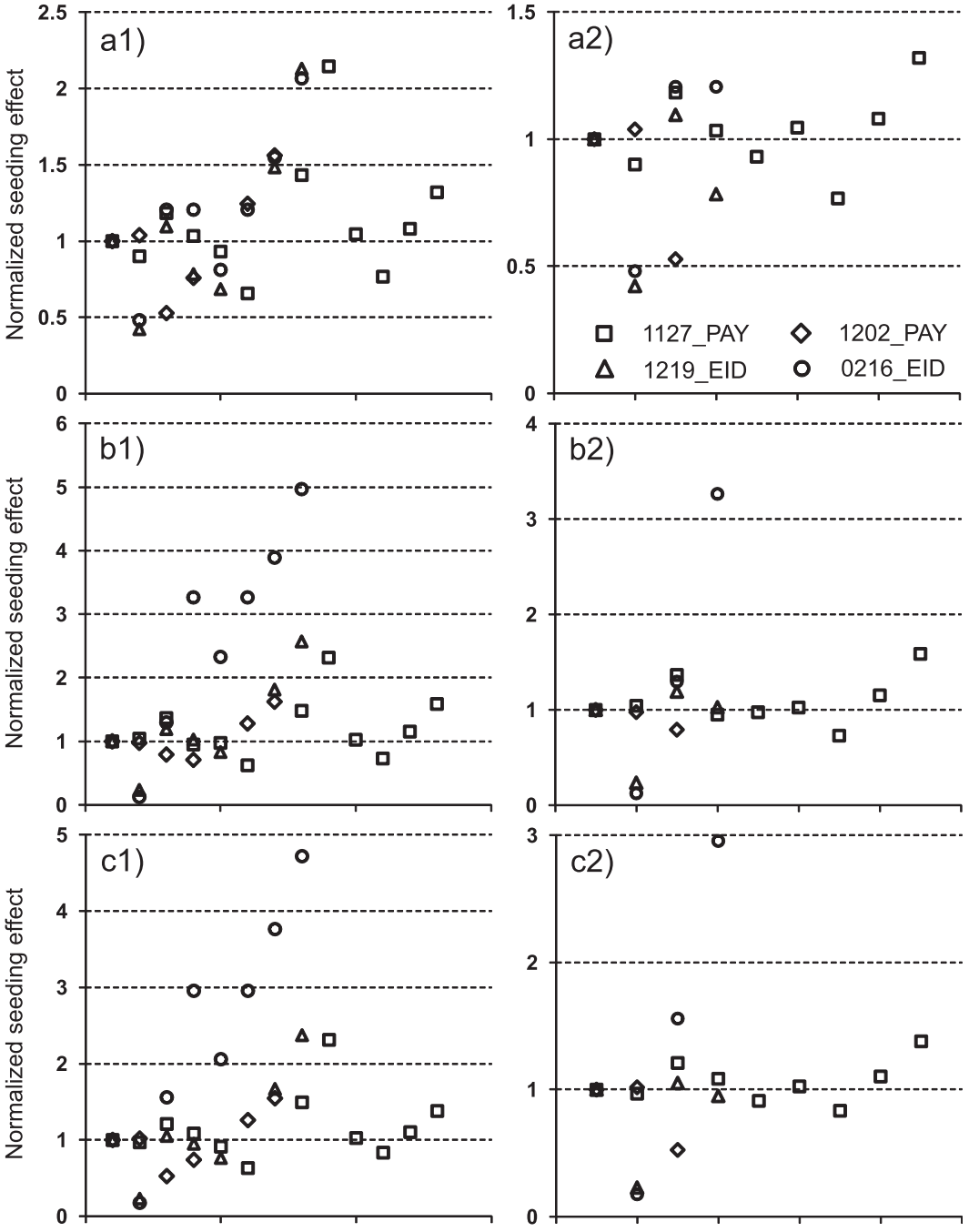

FIG. 9. Scatterplots of normalized seeding effects of all cases (a1) over the entire domain, (b1) over the Snake River basin, and (c1) over the target region. The *X* axis indicates the cases listed in Table 3. (a2),(b2),(c2) As in the left plots, but with the seeding-rate experiments removed.

difference between these two datasets is that the model top of the RTFDDA data (20 hPa, or about 22 km) is significantly higher than the NARR data (100 hPa, or about 16 km). Although such a difference is not very important for wintertime stably stratified orographic cloud simulations, it is critical for summertime deep convection simulations.

The different data top height leads to another interesting point that the vertical grid spacings close to the ground are slightly different in RTFDDA and NARR

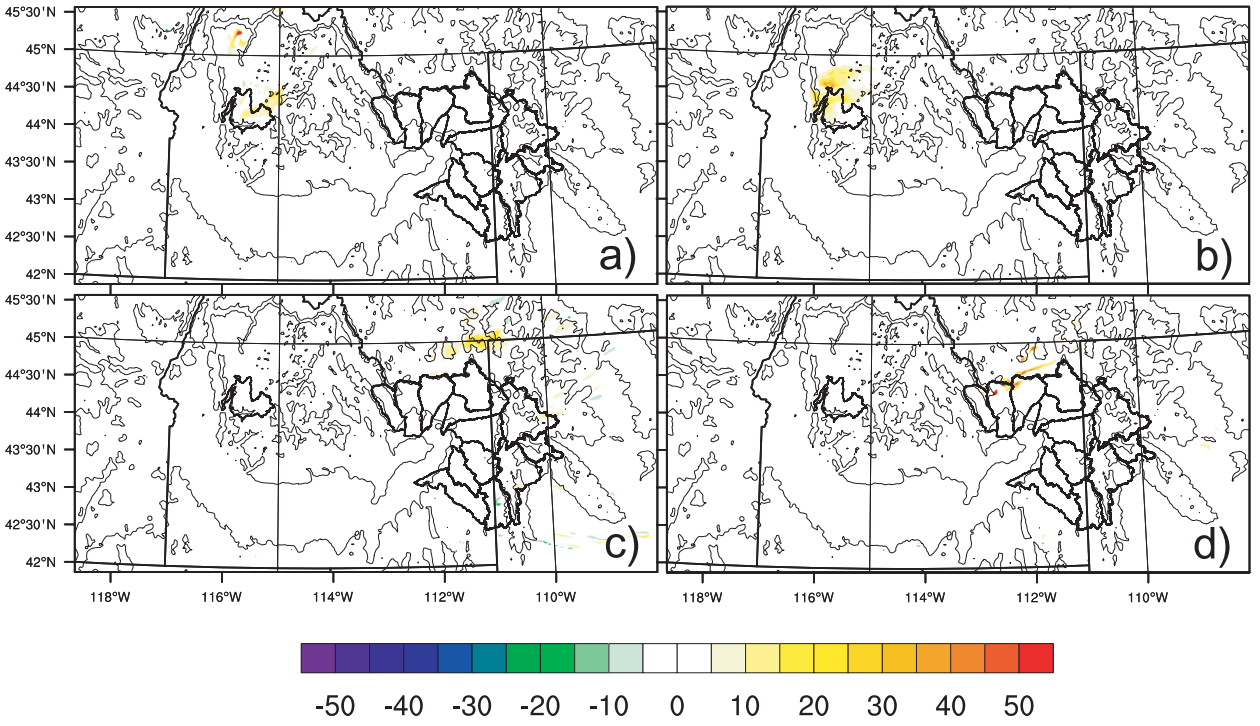

FIG. 10. The local relative precipitation difference (%) between seeding cases and control cases at the end of simulations for (a) 1127_PAY, (b) 1202_PAY, (c) 1219_EID, and (d) 0216_EID.

simulations since the vertical coordinate consists of the same eta levels. The height of the first level above the ground is ~20 m in the RTFDDA runs and is ~17 m in the NARR runs. This phenomenon led us to test how the vertical resolution affects the seeding effects. Several simulations with lower vertical resolution (45 eta levels) showed that the seeding effects became weaker. Since the vertical dispersion of AgI particles from the ground generators is critical to the seeding simulations, higher vertical resolution close to the ground is expected to yield better results. Systematic investigation of the impacts of vertical resolution on seeding effects is subject to another study.

Despite the discrepancy of accumulated precipitation between the NARR control runs and the SNOTEL measurements, we performed the default seeding simulations using the NARR data. The results showed uniformly stronger relative seeding effects than the RTFDDA results did over the domain, the basin, and the target areas for all cases. As both 2D and 3D sensitivity tests demonstrated that the relative seeding effect is inversely related to natural precipitation efficiency, the stronger seeding signals from the NARR simulations were expected since the precipitation amounts of control runs were uniformly less than those of the RTFDDA runs (see Fig. 3). The general patterns of seeding signals were very similar to those of the RTFDDA simulations, indicating consistent seeding effects were simulated regardless of the initial and later boundary conditions being used.

The relative precipitation enhancements of seeding over the entire domain, the Snake basin, and the target areas were small in comparison with the values in Part I (see Table 3 in this study and Tables 2–10 in Part I). This result is mainly due to the differences of precipitation features between the 3D and 2D simulations. The steady state, continuous moisture fluxes, and abundant liquid water content simulated in 2D led to continuously distributed precipitation in one dimension. Such features were not present in 3D simulations. The values in this study represented the ratios between precipitation differences within an area and control precipitation in the same area. Figure 10 shows the local values of the relative precipitation enhancements in percentage (ratios between precipitation differences within one grid box and control precipitation in the same grid box) for all default seeding cases corresponding to Fig. 4. The local values were much higher than those over a large area (~20% in Fig. 10 vs <5% in Table 3). The local values varied from less than −15% (1219_EID) to greater than 50% (1127_PAY and 0216_EID). These highly uncertain local relative seeding signals imply that the seeding effects observed from a single target site are usually not representative for the entire target area. Since the spatial

distribution of precipitation enhancements is not well correlated with natural precipitation patterns, the cloud-seeding effects purely derived from ground-based observations are highly uncertain. A numerical tool similar to the one used here is necessary to help seeding programs quantify the seeding effects over a region.

The 3D setup of this study alleviated the model limitation of 2D simulations. Vertical dispersion and transportation of AgI plumes have been properly handled over the complex terrain in this study. The limitation of constant cloud droplet concentration in the microphysics scheme was still in effect, however. As discussed in Part I, such an assumption affects cloud droplet size, riming efficiency, diffusion, and AgI particle-scavenging processes. Therefore, results of this study need to be interpreted with caution. To better investigate glaciogenic cloud-seeding effects numerically, a more sophisticated microphysics scheme should be used. The microphysics scheme used in this study is efficient and is suitable for real-time forecast application.

5. Conclusions

Four cloud-seeding cases over southern Idaho during the 2010/11 winter season have been simulated by the WRF model using the same AgI cloud-seeding parameterization as was described in Part I. The seeding effects from both ground and airborne seeding and the effects of PBL schemes, seeding rate, seeding timing, seeding location, and cloud microphysical properties on seeding effects have been investigated and compared with those of Part I. The five main conclusions of this study are summarized as follows:

1) For the four cases tested in this study, control simulations driven by the RTFDDA-WRF forecast dataset generated more realistic atmospheric conditions and precipitation patterns than those driven by the NARR dataset.
2) Through the same physical processes as described in Part I, glaciogenic cloud seeding increased the wintertime orographic precipitation by less than 1% over the simulation domain and the Snake River basin and by up to 5% over the target areas. The local values of the relative precipitation enhancements were ~20%. Most of the precipitation enhancements came from vapor depletion.
3) The seeding effect was inversely related to the natural precipitation efficiency but was positively related to seeding rates.
4) Airborne seeding is generally more efficient than ground-based seeding in terms of targeting, but its efficiency depends on meteorological conditions near the target areas.
5) The normalized seeding effects ranged from 0.4 to 1.6 under various conditions for a certain seeding event.

Many of the findings in this study of 3D simulations of actual cloud-seeding events agreed well with those of 2D idealized simulations. With the capability of simulating seeding events in a 3D setup, real-time decision support for seeding operations is now possible. This is a step beyond the suggestions made by the National Research Council (2003) on how numerical models can help weather-modification programs.

Acknowledgments. This study was partly supported by the NCAR Advanced Study Program, the Wyoming Water Development Commission as part of the Wyoming Weather Modification Pilot Program, and Idaho Power Company. The authors greatly appreciate the comments and suggestions of the anonymous reviewers, which significantly improved the quality of the manuscript. All rights to the underlying data collected and/or generated with funding from the Wyoming Water Development Office (WWDO) from which this paper was created remain with the WWDO. This paper does not constitute the opinions of the State of Wyoming, the Wyoming Water Development Commission, or the Wyoming Water Development Office.

REFERENCES

Breed, D., M. Pocernich, R. Rasmussen, B. Boe, and B. Lawrence, 2011: Evaluation of the Wyoming winter orographic cloud seeding program: Design of the randomized seeding experiment. Preprints, *18th Conf. on Planned and Inadvertent Weather Modification,* Seattle, WA, Amer. Meteor. Soc., 2.1. [Available online at https://ams.confex.com/ams/91Annual/webprogram/Paper180664.html.]

Deshler, T., D. W. Reynolds, and A. W. Huggins, 1990: Physical response of winter orographic clouds over the Sierra Nevada to airborne seeding using dry ice or silver iodide. *J. Appl. Meteor.,* **29,** 288–330.

Geerts, B., Q. Miao, Y. Yang, R. Rasmussen, and D. Breed, 2010: An airborne profiling radar study of the impact of glaciogenic cloud seeding on snowfall from winter orographic clouds. *J. Atmos. Sci.,* **67,** 3286–3302.

Givati, A., and D. Rosenfeld, 2005: Separation between cloud-seeding and air-pollution effects. *J. Appl. Meteor.,* **44,** 1298–1314.

Liang, X.-Z., K. E. Kunkel, and A. N. Samel, 2001: Development of a regional climate model for U.S. Midwest applications. Part I: Sensitivity to buffer zone treatment. *J. Climate,* **14,** 4363–4378.

Liu, Y.-B., and Coauthors, 2008: The operational mesogamma-scale analysis and forecast system of the U.S. Army Test and Evaluation Command. Part I: Overview of the modeling system, the forecast products, and how the products are used. *J. Appl. Meteor. Climatol.,* **47,** 1077–1092.

Meyers, M. P., P. J. DeMott, and W. R. Cotton, 1995: A comparison of seeded and nonseeded orographic cloud simulations with an explicit cloud model. *J. Appl. Meteor.,* **34,** 834–846.

National Research Council, 2003: *Critical Issues in Weather Modification Research*. National Academies Press, 131 pp.

Rasmussen, R. M., and Coauthors, 2011: High-resolution coupled climate runoff simulations of seasonal snowfall over Colorado: A process study of current and warmer climate. *J. Climate,* **24,** 3015–3048.

Reisin, T., Z. Levin, and S. Tzivion, 1996: Rain production in convective clouds as simulated in an axisymmetric model with detailed microphysics. Part I: Description of the model. *J. Atmos. Sci.,* **53,** 497–519.

Thompson, G., R. Rasmussen, and K. Manning, 2004: Explicit forecasts of winter precipitation using an improved bulk microphysics scheme. Part I: Description and sensitivity analysis. *Mon. Wea. Rev.,* **132,** 519–542.

——, P. R. Field, W. R. Hall, and R. Rasmussen, 2008: Explicit forecasts of winter precipitation using an improved bulk microphysics scheme. Part II: Implementation of a new snow parameterization. *Mon. Wea. Rev.,* **136,** 5095–5115.

Warner, T. T., R. A. Peterson, and R. E. Treadon, 1997: A tutorial on lateral boundary conditions as a basic and potentially serious limitation to regional numerical weather prediction. *Bull. Amer. Meteor. Soc.,* **78,** 2599–2617.

Wu, W., A. H. Lynch, and A. Rivers, 2005: Estimating the uncertainty in a regional climate model related to initial and lateral boundary conditions. *J. Climate,* **18,** 917–933.

Xue, L., A. Teller, R. M. Rasmussen, I. Geresdi, and Z. Pan, 2010: Effects of aerosol solubility and regeneration on warm-phase orographic clouds and precipitation simulated by a detailed bin microphysical scheme. *J. Atmos. Sci.,* **67,** 3336–3354.

——, ——, ——, ——, ——, and X. Liu, 2012: Effects of aerosol solubility and regeneration on mixed-phase orographic clouds and precipitation. *J. Atmos. Sci.,* **69,** 1994–2010.

——, and Coauthors, 2013: Implementation of a silver iodide cloud-seeding parameterization in WRF. Part I: Model description and idealized 2D sensitivity tests. *J. Appl. Meteor. Climatol.,* **52,** 1433–1457.